Journal of Electroanalytical Chemistry 829 (2018) 81–87

Contents lists available at ScienceDirect

Journal of Electroanalytical Chemistry

journal homepage: www.sciencedirect.com/journal/journal-of-electroanalytical-chemistry

Two-dimensional nickel hydroxide nanosheets with high-content of nickel (III) species towards superior urea electro-oxidation

Dongsheng Wang[a], Siwen Liu[a], Qiuping Gan[a], Jianniao Tian[a], Tayirjan Taylor Isimjan[b], Xiulin Yang[a,*]

[a] Key Laboratory for the Chemistry and Molecular Engineering of Medicinal Resources (Ministry of Education of China), College of Chemistry and Pharmacy, Guangxi Normal University, Guilin 541004, PR China
[b] Saudi Arabia Basic Industries Corporation (SABIC) at King Abdullah University of Science and Technology (KAUST), Saudi Arabia

ARTICLE INFO

Keywords:
$Ni(OH)_2$ sheets
Ni(III) rich
Two-dimensional
Electrocatalysis
Urea electro-oxidation

ABSTRACT

Development of high-efficient and stable electrocatalysts for urea oxidation reaction (UOR) is of a great challenge due to the sluggish kinetics of $6e^-$ transfer process. Here, we have developed a facile and easy-to-scale approach to fabricate two-dimensional Ni(III)-rich $Ni(OH)_2$ nanosheets on amine-functionalized carbon (Ni^{3+}-rich $Ni(OH)_2/C\text{-}NH_2$). Morphological characterizations confirm the existence of nanosheets, and XPS spectra indicate that the content of Ni^{3+} species in Ni^{3+}-rich $Ni(OH)_2/C\text{-}NH_2$ (ca. 57.6%) is significantly higher than that of in $Ni(OH)_2/C\text{-}NH_2$ (ca. 43.1%) and $Ni(OH)_2/C$ (ca. 20.7%). Electrochemical analyses illustrate that the as-prepared Ni^{3+}-rich $Ni(OH)_2/C\text{-}NH_2$ catalyst exhibits the highest current density (91.72 mA cm^{-2}) at a potential of 0.61 V, which is 2.06-, 2.08- and 3.47-fold higher than that of $Ni(OH)_2/C\text{-}NH_2$, $Ni(OH)_2/C$ and Pt/C, respectively. Moreover, the Ni^{3+}-rich $Ni(OH)_2/C\text{-}NH_2$ catalyst also demonstrates an outstanding voltammetric cycles and long-term chronoamperometric stability. The superior electrocatalytic activity and stability could be ascribed to the synergistic effect of Ni^{3+} doping as well as the amine-functionalized carbon, where higher concentration Ni^{3+} species in $Ni(OH)_2$ sheets could provide more active sites for adsorption and transformation of urea molecules, while fluffy $C\text{-}NH_2$ support could enhance the ability of solute diffusion, electron transport and gas emissions, thereby dramatically improve the catalytic activity.

1. Introduction

The demands for sustainable green energy and zero-tolerance on environmental pollution have emerged as typical themes of social and economic development [1,2]. The recent studies show that 2–2.5% urea contaminated wastewaters were released from various industrial streams [3]. The presence of urea in wastewater streams is a serious problem since it is eventually hydrolyzed into ammonia, which results increasing pH of the soil as well as contributing to the greenhouse effect when it is released to the atmosphere [4]. Consequently, it is of great significance to eliminate the environmental pollution of urea from the source. A wide range of processes has been investigated in this regards including electrochemical oxidation, physical adsorption, and biological decomposition [5–7]. Most of these approaches require complicated equipment and a high-energy input thereof limited at industrial application. Direct urea fuel cells (DUFC) has been shown to be a promising approach since it converts urea into N_2 and CO_2 while generating electricity [8]. However, the challenge lays on how to overcome the sluggish kinetics of $6e^-$ electron transfer [9]. The elemental doping approaches were proven to be one of the effective strategies deal with this kind of problems in the fields of water splitting [10–12], fuel cells [13–15], photocatalysis [16–18], gas capture [19,20], and so on. In general, doping a hetero-element inevitably increases the structural defects, which in turn leads to the degradation of the catalytic performance [21,22]. Conversely, homo-species doping, where the same element with different chemical states is incorporated into the crystal lattice, considered to be a very promising strategy for enhancing catalytic performance because it does not cause significant structural distortion thereof less defects compared to the heterogeneous doping [17]. Although there are two types of catalysts based on Ni and Mn elements which are being used for urea oxidation, Ni-based catalyst is more preferred over Mn-based catalysts because Mn-based catalyst requires higher overpotential and shows less efficiency [23,24] compare to that of Ni-based catalysts [25–27]. It is a well acknowledged fact that Ni $(OH)_2$ to NiOOH is the critical step before electrocatalytic urea oxidation ($Ni(OH)_2 + OH^- \rightarrow NiOOH + H_2O + e^-$) [27]. Furthermore,

* Corresponding author.
E-mail addresses: isimjant@sabic.com (T.T. Isimjan), xiulin.yang@kaust.edu.sa (X. Yang).

https://doi.org/10.1016/j.jelechem.2018.10.007
Received 19 June 2018; Received in revised form 22 September 2018; Accepted 5 October 2018
Available online 06 October 2018
1572-6657/

calculations also show that urea molecules are more easily adsorbed onto the surface of NiOOH species [28]. In other words, increasing NiOOH content in the catalyst should significantly improve the catalytic performance of urea oxidation. To the best of our knowledge, there are rarely reports in this regard, including exfoliated nickel hydroxide nanosheets [29], S-doped $Ni(OH)_2$ [9], α-$Ni(OH)_2$@CNT [30], etc. Therefore, exploring the effect of NiOOH species in homogeneous catalyst for urea electro-oxidation is still of great significance.

Herein, we report a facile method of doping of Ni^{3+} species in 2D $Ni(OH)_2$ sheets by ammonia evaporation assisted method in the presence of $Ni(NO_3)_2$ and XC-72 carbon. The as-prepared Ni^{3+}-rich $Ni(OH)_2$/C-NH_2 catalyst exhibits the highest catalytic activity towards urea electro-oxidation in alkaline solution, which is 2.06-, 2.08- and 3.47-fold higher than $Ni(OH)_2$/C-NH_2, $Ni(OH)_2$/C and Pt/C, respectively. Moreover, the Ni^{3+}-rich $Ni(OH)_2$/C-NH_2 catalyst also exhibits an outstanding stability in 1.0 M KOH + 0.33 M urea solution for continuous running of 2.0 h. The superior catalytic activity and stability could be ascribed to the presence of NiOOH spaces through Ni^{3+} doping in the β phase of 2D $Ni(OH)_2$ sheets as well as the synergistic effect between $Ni(OH)_2$ and amine-factionalized carbon support. The catalytic mechanism of the hybrid catalyst for urea electro-oxidation has also been proposed and discussed in detail in this work.

2. Experimental

2.1. Synthesis of Ni^{3+}-rich $Ni(OH)_2$/C-NH_2

All chemical reagents are analytical grade and used without further purification. 313.6 mg $Ni(NO_3)_2{\cdot}6H_2O$ and 100 mg XC-72 carbon were dispersed into a mixture solution (40 mL $NH_3{\cdot}H_2O$ + 30 mL H_2O + 10 mL ethanol) in a glass beaker. After sonicating for 30 min and subsequently stirred for 4 h. The resulted mixture solution was heated to 120 °C to evaporate the solvent without stirring for several hours. The residual product was collected, washed three times with H_2O-ethanol mixture and then freeze dried at − 37 °C for 12 h. The resulting products were labeled as Ni^{3+}-rich $Ni(OH)_2$/C-NH_2. For better comparison, the $Ni(OH)_2$/C-NH_2 was prepared under the same condition as above without the simultaneous heating and no stirring.

The $Ni(OH)_2$/C was prepared as follows, 313.6 mg $Ni(NO_3)_2{\cdot}6H_2O$ and 100 mg XC-72 carbon were added into a mixture solution of 15 mL H_2O and 5 mL ethanol. After sonicated for 30 min, 20 mL of 0.107 M NaOH solution was dropped slowly under vigorously stirring. Four hours later, the products were centrifuged, washed with a water-ethanol mixture, and then freeze dried. The pure $Ni(OH)_2$ was purchased from Macklin biochemical company.

2.2. Catalyst characterizations

X-ray diffraction (XRD) pattern was detected by a Rigaku D/Max 2500/PC with Cu Kα radiation. Scanning electron microscopy (SEM, Quanta FEG 200) with EDS (energy dispersive X-ray spectroscopy) and transmission electron microscopy (TEM, JEOL, JEM-2100F) were used to investigate the morphologies and microstructures of the designed materials. X-ray photoelectron spectroscopy (XPS, ESCALAB 250Xi) was used to detect the chemical states of the designed materials. Thermogravimetric analysis (TGA) was used to analyze the loading of the inorganic materials in the hybrid composites.

2.3. Electrochemical measurements

Biologic VMP3 electrochemical workstation was operated to measure all the electrochemical data, in which saturated calomel electrode (SCE), Pt sheet (1 cm × 2 cm) and glassy carbon electrode (GCE, ϕ = 3 mm) were used as the reference, counter and working electrodes, respectively. The GCE was polished to a mirror-like surface by α-Al_2O_3 powder with different sizes. The surface was thoroughly washed with copious acetone, ethanol, and H_2O. 2.0 mg samples were dissolved in a mixture solution (400 μL) of H_2O and ethanol with a volume ratio of 1:1. After ultrasonicated for 30 min, 28 μL of the suspension was dropped onto the polished GCE surface. Then, 5 μL of 0.5% Nafion solution was pipetted to fix the catalyst on the electrode surface. The loading of $Ni(OH)_2$ was kept at ca. 1.0 mg cm^{-2} for all the catalysts.

The electrochemical performances of all the catalysts were evaluated in N_2-saturated 1.0 M KOH and 1.0 M KOH + 0.33 M urea solution. Cyclic voltammetry (CV) was conducted in the range of 0 to 0.5 V in N_2-saturated 1.0 M KOH solution and operated in the range of 0 to 0.8 V in N_2-saturated 1.0 M KOH + 0.33 M urea solution. The long-term stability of different catalysts was tested at a fixed potential in N_2-saturated 1.0 M KOH + 0.33 M urea for 7200 s. All the electrochemical results are respect to the SCE reference and all the experiments were carried out at room temperature (25 ± 0.5 °C).

3. Results and discussion

3.1. Crystal structures and morphology characterizations

X-ray diffraction (XRD) patterns are initially used to track the crystal structures of as-prepared Ni^{3+}-rich $Ni(OH)_2$/C-NH_2, $Ni(OH)_2$/C-NH_2 and $Ni(OH)_2$/C materials. As shown in Fig. 1a, we can see that the three samples show similar peaks in the range of 10° to 90°, which are consistent with the typical diffraction peaks of β-$Ni(OH)_2$ (JCPDS: 14-0117) [31]. It is noteworthy that the diffraction peaks of Ni^{3+}-rich $Ni(OH)_2$/C-NH_2 are much higher and stronger than that of others, indicating better crystallinity. Moreover, there are two additional peaks at ~25.0° and 44.4° can be attributed to the hexagonal phase of carbon (002) and (101), respectively [32]. Specially, there is a typical peak at 12.7° in 2D Ni^{3+}-rich $Ni(OH)_2$/C-NH_2 spectrum, which is corresponding to the crystal facet (003) of NiOOH (JCPDS: 06-0075), indicating that the Ni^{3+} species are well-doped in $Ni(OH)_2$ structures.

The morphology of the synthesized materials is identified by scanning electron microscopy (SEM) and transmission electron microscopy (TEM). As shown in Fig. 1b, we can see that the sheet-like structural Ni^{3+}-rich $Ni(OH)_2$ and amine functionalized carbon support are randomly distributed in the whole range, and the Ni^{3+}

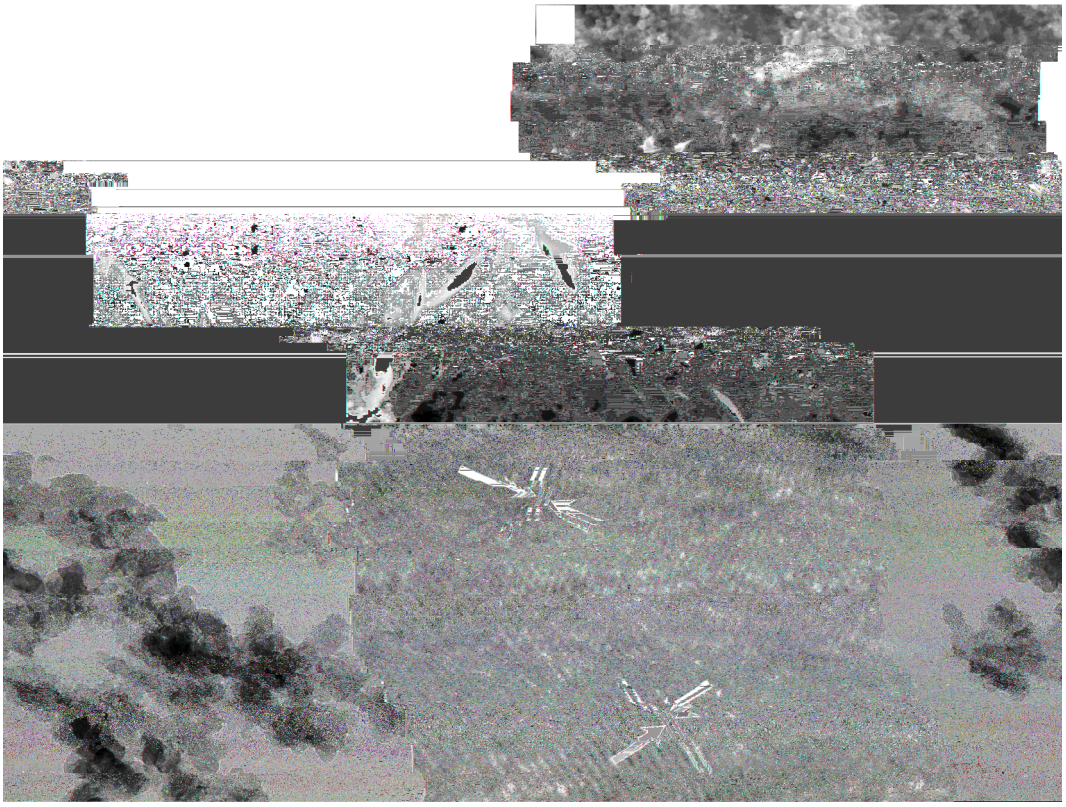

Fig. 1. (a) XRD patterns of Ni^{3+}-rich $Ni(OH)_2$/C-NH_2, $Ni(OH)_2$/C-NH_2 and $Ni(OH)_2$/C. (b) SEM image of the synthesized Ni^{3+}-rich $Ni(OH)_2$/C-NH_2. (c) TEM and (d) high-resolution TEM images of Ni^{3+}-rich $Ni(OH)_2$/C-NH_2.

855.3 and 856.5 eV are corresponding to $Ni(OH)_2$ and NiOOH, respectively [35]. We can see that the contents of NiOOH species in the hybrid catalysts are in the order of Ni^{3+}-rich $Ni(OH)_2$/C-NH_2 (ca. 57.6%) > $Ni(OH)_2$/C-NH_2 (ca. 43.1%) > $Ni(OH)_2$/C (ca. 20.7%), indicating that the Ni^{3+} species are much easier to be formed under steady-state conditions in ammonia solution at 120 °C. Furthermore, the

Fig. 2. (a) High-resolution Ni $2p_{3/2}$ XPS spectrum of Ni^{3+}-rich $Ni(OH)_2$/C-NH_2, $Ni(OH)_2$/C-NH_2 and $Ni(OH)_2$/C. (b) High-resolution N 1s XPS spectrum of Ni^{3+}-rich $Ni(OH)_2$/C-NH_2. (c) Thermogravimetric (TG) analysis of Ni^{3+}-rich $Ni(OH)_2$ and Ni^{3+}-rich $Ni(OH)_2$/C-NH_2 in O_2

Fig. 3. Consecutive cyclic voltammograms (CVs) of (a) Ni^{3+}-rich $Ni(OH)_2$/C-NH_2 and (b) $Ni(OH)_2$/C catalysts in N_2-saturated 1.0 M KOH solution with a scan rate of 30 mV s^{-1}. (c) The extracted second cycles from CVs of the synthesized three samples. (d) CVs of Ni^{3+}-rich $Ni(OH)_2$/C-NH_2 catalyst in N_2-saturated 1.0 M KOH with different scan rates in the range of 10 to 100 mV s^{-1}. (e) Peak current densities versus the scan rates (10–40 mV s^{-1}) of Ni^{3+}-rich $Ni(OH)_2$/C-NH_2 catalyst. (f) The peak current densities versus square roots of synthesized different catalysts in the range of 50 to 100 mV s^{-1}.

high-resolution N 1 s spectrum is also detected and assigned to amino-N (399.1 eV) and residual nitrate (406.3 eV), respectively (Fig. 2b) [36]. As shown in Fig. S3, the elements of C, N, O, and Ni exist in Ni^{3+}-rich $Ni(OH)_2$/C-NH_2 material, in which the high-resolution C 1s spectrum are convoluted to C═C (284.0 eV), C—C (284.8 eV), C—O (286.0 eV) and C═O (288.5 eV), respectively [37]. In addition, the material transformations in the hybrid material are analyzed by thermogravimetric (TG) analysis in the O_2 atmosphere. We can see that there are two strong exothermic peaks at 317 °C and 432 °C (Fig. S4), which are corresponding to the dehydration of $Ni(OH)_2$ and combustion of carbon, respectively. Moreover, according to the TG analysis with or without carbon support (Fig. 2c), we can easily conclude that the loading contents of Ni^{3+}-rich $Ni(OH)_2$ in the hybrid material is ca. 50.2 wt%, which is consistent with the theoretical result (50.0 wt%).

3.3. Electrochemical analysis

Electrochemical studies are performed in order to evaluate the transformation of constituent species in the hybrid catalysts in 1.0 M KOH solution. Each solution was purged with high-purity N_2 gas for 15 min at room temperature before the measurements. As shown in Fig. 3a, the consecutive CV curves of Ni^{3+}-rich $Ni(OH)_2$/C-NH_2 catalyst are recorded in the range of 0 to 0.5 V with a scan rate of 30 mV s^{-1} for different cycles. A pair of redox peaks were observed on Ni^{3+}-rich Ni $(OH)_2$/C-NH_2 catalyst due to the interconversion of $Ni(OH)_2$ and NiOOH ($Ni(OH)_2 + OH^- \leftrightarrow NiOOH + H_2O + e^-$) [38,39]. In the consecutive CVs, the peak intensity increases gradually with the increase of the number of cycles, while the current enhancements are considered to be the progressive enrichment of the accessible electroactive species (Ni^{2+} and Ni^{3+}) on or near the surface [40]. In addition, the peak potentials are almost same, suggesting no phase transformation of NiOOH from β to γ occurred during the measurements. Meaning, a high catalytic performance can be expected from this material since the β-NiOOH phase is proven to have a superior electrochemical performance in alkaline solution [40]. In contrary, the current densities of $Ni(OH)_2$/C-NH_2 declined gradually with increasing number of CV cycles owing to the agglomerations during the reaction (Fig. S5). The $Ni(OH)_2$/C catalyst shows an apparently negative shifts both at anodic and cathodic peak potentials with increasing number of CV cycles (Fig. 3b), which was resulted from the physical transformations of $Ni(OH)_2$ species when the γ-NiOOH and α-$Ni(OH)_2$ phases have coexisted under steady-state conditions [41]. The coexistence of γ-NiOOH with α-$Ni(OH)_2$ species is associated with swelling or volume expansion of the catalyst, therefore, causes microcracks and disintegrates, and subsequently increases the internal resistance and reduces the catalyst efficiency [42].

The electrochemically active surface area (ESA) of the three samples are further investigated through the cathodic reduction peaks of NiOOH species to $Ni(OH)_2$ on the catalyst surface from the backward scan [28,43], The peak intensity is proportional to the number of active sites exposed for urea electro-oxidation. The ESA of different catalysts are calculated using the equation of ESA = Q / mq, where Q is the amount of total charge requested to reduce NiOOH to $Ni(OH)_2$, m is the amount of Ni in the hybrid catalysts, and q is 257 μC cm^{-2}. As shown in Fig. S5, the ESA values are 88.6, 83.6 and 217.2 m^2 g^{-1} for Ni^{3+}-rich $Ni(OH)_2$/C-NH_2, $Ni(OH)_2$/C-NH_2 and $Ni(OH)_2$/C respectively, indicating the crucial role of β-$Ni(OH)_2$ phase on urea electrooxidation.

Fig. 3d presents the CV curves of Ni^{3+}-rich $Ni(OH)_2$/C-NH_2 catalyst with different scan rates (10–200 mV s^{-1}) in 1.0 M KOH solution. The peak potentials and peak current densities rise gradually with increasing the scan rates. The peak current densities are proportional to the scan rates in the range of 10–40 mV s^{-1}, originating from the electrochemical activity of the surface redox couple (Fig. 3e) [40]. According to the equation of $I_p = (n^2F^2 / 4RT)\upsilon A\Gamma^*$, where Γ^* is the surface coverage of the redox species and υ is the scan rate [44], it can be inferred that the Γ^* value is proportional to the slope. Thus, the total redox species of different materials are in the order of $Ni(OH)_2$/C > Ni^{3+}-rich $Ni(OH)_2$/C-NH_2 > $Ni(OH)_2$/C-NH_2. In the higher scan rates (Fig. 3f), peak current densities are proportional to the square roots of higher scan rates (50–100 mV s^{-1}), indicating that the diffusion controlled processes dominate the chemical reaction [44].

Generally, more redox species on catalyst surface can achieve higher catalytic performance. As shown in Fig. 4a, the Ni^{3+}-rich $Ni(OH)_2$/C-

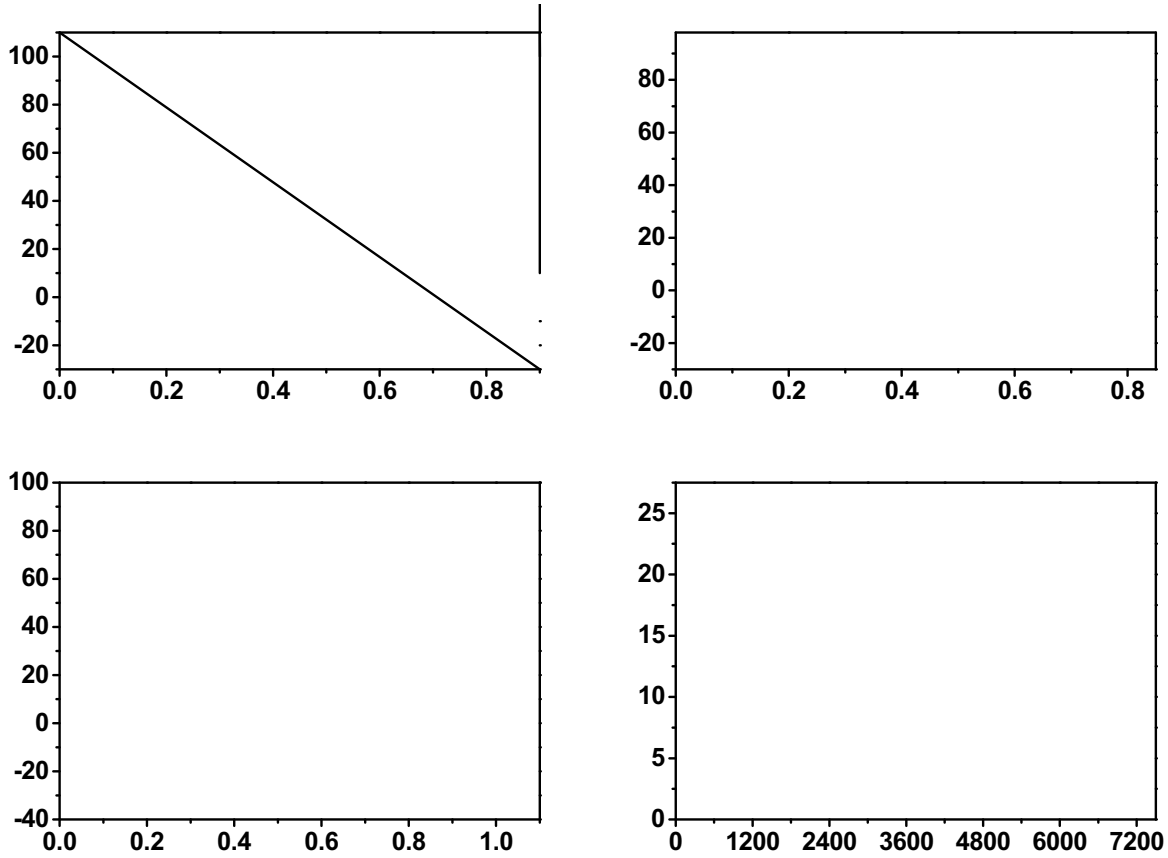

Fig. 4. (a) CVs of different catalysts conducted in 1.0 M KOH + 0.33 M urea solution with a scan rate of 50 mV s^{-1}. Repeated CVs of Ni^{3+}-rich $Ni(OH)_2$/C-NH_2 catalyst in 1.0 M KOH + 0.33 M urea solution under (b) static testing condition and (c) rotating disk electrode with 1600 rpm at a scan rate of 50 mV s^{-1}. (D) Chronoamperometric curves of different catalysts at a fixed potential of 0.35 V in 1.0 M KOH + 0.33 M urea solution.

NH_2 catalyst exhibits an onset potential at ca. 0.33 V, which is slightly lower than that of $Ni(OH)_2$/C-NH_2 at ca. 0.31 V, meanwhile notably higher than those of $Ni(OH)_2$/C-NH_2 at ca. 0.36 V, Ni^{3+}-rich $Ni(OH)_2$ at ca. 0.37 V and Pt/C at ca. 0.34 V. After that, the current densities increase gradually with increase of the applied potentials until reach the peak potentials. As a result, the Ni^{3+}-rich $Ni(OH)_2$/C-NH_2 catalyst shows the highest current density (91.71 mA cm^{-2}) during the forward scan in urea electro-oxidation. The resulting current density is 2.06-, 2.08-, 3.47- and 2.89-fold higher than that of $Ni(OH)_2$/C-NH_2 (44.53 mA cm^{-2}), $Ni(OH)_2$/C (44.01 mA cm^{-2}), Pt/C (26.41 mA cm^{-2}) and Ni^{3+}-rich $Ni(OH)_2$ (31.76 mA cm^{-2}), respectively. The greatly improved current density of Ni^{3+}-rich $Ni(OH)_2$/C-NH_2 catalyst can be ascribed to the stable 2D structures exposing more active sites and more β-NiOOH species on the surface rather than γ-NiOOH species. Besides, the fluffy C-NH_2 support also plays an important role in improving the catalytic activity due to the increasing of solute diffusion, electron transport, and final gas emissions. A slight degradation of catalytic activity after peak potentials and lower reverse current densities can be caused by the gas bubbles of the final products (e.g., CO_2, N_2) blocking the active sites during the reaction, which subsequently inhibit the adsorption of urea molecules from the electrolyte. Fig. 4b shows the continuous CV curves for 100 cycles in 1.0 M KOH + 0.33 M urea solution with a scan rate of 50 mV s^{-1}. We can see that the peak current densities of Ni^{3+}-rich $Ni(OH)_2$/C-NH_2 catalyst decrease gradually with increasing the number of cycles. However, the current densities are stable when we conduct the UOR using rotating disk electrode with 1600 rpm during the CV cycles from 1st to 100th (Fig. 4c). This could be due to the removing gas bubble on the surface and expose the active sides for urea oxidation.

In order to evaluate the long-term stability of these catalysts for urea oxidation, the chronoamperometric measurements are performed at a constant potential (0.35 V) in 1.0 M KOH + 0.33 M urea solution at 25 °C for 120 min. Although the current densities of all the catalysts decrease rapidly at the initial stage as shown in Fig. 4d, the Ni^{3+}-rich Ni $(OH)_2$/C-NH_2 catalyst shows the highest initial and final current densities in the whole process. This catalyst demonstrates promising activities for UOR application [9].

3.4. Catalytic mechanism

The entire catalytic process of Ni^{3+}-rich $Ni(OH)_2$/C-NH_2 catalyst for urea electro-oxidation could be explained as following three steps (Fig. 5a–b). (1) Adsorption of urea molecules and OH^- ions to the active sites of Ni^{3+}-doped $Ni(OH)_2$ sheets. (2) Gradual oxidation of $Ni(OH)_2$ species on the catalyst surface into NiOOH species ($Ni(OH)_2 + OH^- \leftrightarrow NiOOH + H_2O + e^-$) [45]. (3) The urea oxidation by NiOOH to N_2 and CO_2 molecules while itself becoming $Ni(OH)_2$ to complete the catalytic cycle. As discussed above, the two-dimensional Ni^{3+}-rich $Ni(OH)_2$ sheets reported here is mainly transformed into β-NiOOH species rather than γ-NiOOH species and yet the Ni^{3+}-rich $Ni(OH)_2$/C-NH_2 catalyst shows the highest catalytic activity for urea electro-oxidation among all the other catalysts. Therefore, it can be concluded that β-NiOOH species have higher catalytic activity for urea electro-oxidation in alkaline solution than γ-NiOOH species. Furthermore, the amine groups on the carbon support not only improved surface attachment of $Ni(OH)_2$ but also attracting the reactant through hydrogen bonding. In addition, it also facilitated the directional conversion of β-$Ni(OH)_2$ species to β-NiOOH species. Finally, we believe that the high concentration of β-

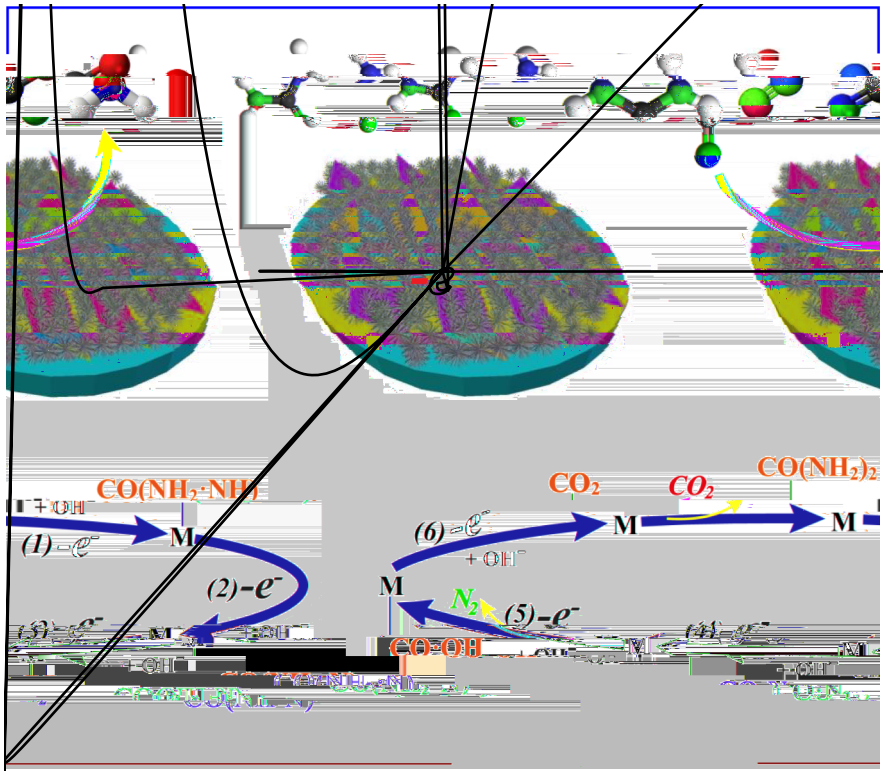

Fig. 5. (a) Schematic description of the transformation of $Ni(OH)_2$ and NiOOH species and their electro-oxidation of urea on the surface of Ni^{3+}-rich $Ni(OH)_2$/C-NH_2 catalyst in alkaline solution. (b) Catalytic mechanism diagram of the formed NiOOH species on the hybrid catalyst surface for electrocatalytic oxidation of urea molecules in alkaline solution.

NiOOH species and the synergy between catalyst and support are the two main reasons for the better catalytic performance.

4. Conclusion

In summary, we have developed a facile approach to fabricate 2D Ni^{3+}-rich $Ni(OH)_2$ sheets on amine functionalized carbon. The as-prepared catalyst exhibits an enhanced electrocatalytic activity and excellent durability for urea electro-oxidation in alkaline solution compared to $Ni(OH)_2$/C-NH_2, $Ni(OH)_2$/C, Pt/C and Ni^{3+}-rich $Ni(OH)_2$ catalysts. This superior electrocatalytic performance towards the urea electro-oxidation could be ascribed to the higher concentration of β-NiOOH intermediated and the synergistic effect of Ni^{3+} species doping, 2D structural $Ni(OH)_2$ sheets and amine functionalized carbon in the hybrid catalyst. Besides, considering the low cost of carbon and Ni salt, the 2D structural Ni^{3+}-rich $Ni(OH)_2$/C-NH_2 catalyst may have practical applications in DUFC and other areas (e.g., lithium battery, water splitting, etc.).

Acknowledgments

This work has been supported by the National Natural Science Foundation of China (21363003, 21165004, 21163002), Natural Science Foundation of Guangxi Province (2014GXNSFGA118008, 2014GXNSFFA118003), BAGUI scholar program (2014A001) and Project of Talents Highland of Guangxi Province.

Notes

The authors declare no competing financial interest.

Appendix A. Supplementary data

Figs. S1–S6 and Tables S1 give more details on characterization of our synthesized materials and their electrocatalytic performance data; additional SEM, XPS, TG, and electrocatalytic performance data (PDF).

Supplementary data to this article can be found online at https://doi.org/10.1016/j.jelechem.2018.10.007.

References

[1] Y.P. Xie, Y. Yang, G. Wang, G. Liu, Oxygen vacancies promoted interfacial charge carrier transfer of CdS/ZnO heterostructure for photocatalytic hydrogen generation, J. Colloid Interface Sci. 503 (2017) 198–204.
[2] D. Yoon, J. Lee, B. Seo, B. Kim, H. Baik, S.H. Joo, K. Lee, Cactus-like hollow $Cu_{2-x}S$@Ru nanoplates as excellent and robust electrocatalysts for the alkaline hydrogen evolution reaction, Small 13 (2017) 1700052.
[3] R. Lan, S. Tao, J.T.S. Irvine, A direct urea fuel cell-power from fertiliser and waste, Energy Environ. Sci. 3 (2010) 438–441.
[4] S.L. Luo, Y. Li, L.X. Yang, C.B. Liu, F. Su, Y. Chen, Low-temperature, facile fabrication of ultrafine Cu_2O networks by anodization on TiO_2 nanotube arrays, Semicond. Sci. Technol. 27 (2012) 105010.
[5] R. Ding, L. Qi, M. Jia, H. Wang, Facile synthesis of mesoporous spinel $NiCo_2O_4$ nanostructures as highly efficient electrocatalysts for urea electro-oxidation, Nanoscale 6 (2014) 1369–1376.
[6] J. Liu, X. Chen, Z. Shao, P. Zhou, Preparation and characterization of chitosan/Cu (II) affinity membrane for urea adsorption, J. Appl. Polym. Sci. 90 (2003) 1108–1112.
[7] L. Hu, J. Luo, D. Lu, Q. Tang, Urea decomposition: efficient synthesis of pyrroles using the deep eutectic solvent choline chloride/urea, Tetrahedron Lett. 59 (2018) 1698–1701.
[8] G. Wang, Y. Ling, X. Lu, H. Wang, F. Qian, Y. Tong, Y. Li, Solar driven hydrogen releasing from urea and human urine, Energy Environ. Sci. 5 (2012) 8215–8219.
[9] X. Zhu, X. Dou, J. Dai, X. An, Y. Guo, L. Zhang, S. Tao, J. Zhao, W. Chu, X.C. Zeng, C. Wu, Y. Xie, Metallic nickel hydroxide nanosheets give superior electrocatalytic oxidation of urea for fuel cells, Angew. Chem. Int. Ed. 55 (2016) 12465–12469.
[10] H. Lin, N. Liu, Z. Shi, Y. Guo, Y. Tang, Q. Gao, Cobalt-doping in molybdenum-carbide nanowires toward efficient electrocatalytic hydrogen evolution, Adv. Funct. Mater. 26 (2016) 5581.
[11] X. Zhong, Y. Sun, X. Chen, G. Zhuang, X. Li, J.-G. Wang, Mo doping induced more active sites in urchin-like $W_{18}O_{49}$ nanostructure with remarkably enhanced performance for hydrogen evolution reaction, Adv. Funct. Mater. 26 (2016) 5778–5786.
[12] T. Liu, X. Ma, D. Liu, S. Hao, G. Du, Y. Ma, A.M. Asiri, X. Sun, L. Chen, Mn doping of CoP nanosheets array: an efficient electrocatalyst for hydrogen evolution reaction with enhanced activity at all pH values, ACS Catal. 7 (2016) 98–102.
[13] T. Palaniselvam, M.O. Valappil, R. Illathvalappil, S. Kurungot, Nanoporous graphene by quantum dots removal from graphene and its conversion to a potential oxygen reduction electrocatalyst via nitrogen doping, Energy Environ. Sci. 7 (2014) 1059–1067.
[14] H.-W. Liang, X. Zhuang, S. Brüller, X. Feng, K. Müllen, Hierarchically porous carbons with optimized nitrogen doping as highly active electrocatalysts for oxygen

reduction, Nat. Commun. 5 (2014) 4973.
[15] M. Al-Mamun, Z. Zhu, Y. Huajie, X. Su, H. Zhang, P. Liu, H. Yang, D. Wang, Z. Tang, Y. Wang, H. Zhao, Surface sulfur doping induced enhanced performance of cobalt catalysts in oxygen evolution reactions, Chem. Commun. 52 (2016) 9450–9453.
[16] Z. Zhang, X. Yang, M.N. Hedhili, E. Ahmed, L. Shi, P. Wang, Microwave-assisted self-doping of TiO_2 photonic crystals for e□cient photoelectrochemical water splitting, ACS Appl. Mater. Interfaces 6 (2014) 691–696.
[17] Z. Zhang, M.N. Hedhili, H. Zhu, P. Wang, Electrochemical reduction induced self-doping of Ti^{3+} for e□cient water splitting performance on TiO_2 based photoelectrodes, Phys. Chem. Chem. Phys. 15 (2013) 15637–15644.
[18] R. Franking, L. Li, M.A. Lukowski, F. Meng, Y. Tan, R.J. Hamers, S. Jin, Facile post-growth doping of nanostructured hematite photoanodes for enhanced photoelectrochemical water oxidation, Energy Environ. Sci. 6 (2013) 500–512.
[19] W. Tian, H. Zhang, H. Sun, A. Suvorova, M. Saunders, M. Tade, S. Wang, Heteroatom (N or N-S)-doping induced layered and honeycomb microstructures of porous carbons for CO_2 capture and energy applications, Adv. Funct. Mater. 26 (2016) 8651–8661.
[20] B. Zhu, K. Qiu, C. Shang, Z. Guo, Naturally derived porous carbon with selective metal- and/or nitrogen-doping for e□cient CO_2 capture and oxygen reduction, J. Mater. Chem. A 3 (2015) 5212–5222.
[21] A. Naldoni, M. Allieta, S. Santangelo, M. Marelli, F. Fabbri, S. Cappelli, C.L. Bianchi, R. Psaro, V. Dal Santo, E□ect of nature and location of defects on bandgap narrowing in black TiO_2 nanoparticles, J. Am. Chem. Soc. 134 (2012) 7600–7603.
[22] H.M. Chen, C.K. Chen, R.-S. Liu, L. Zhang, J. Zhang, D.P. Wilkinson, Nano-architecture and material designs for water splitting photoelectrodes, Chem. Soc. Rev. 41 (2012) 5654–5671.
[23] S. Chen, J. Duan, A. Vasile□, S.Z. Qiao, Size fractionation of two-dimensional sub-nanometer thin manganese dioxide crystals towards superior urea electrocatalytic conversion, Angew. Chem. Int. Edit. 55 (2016) 3804–3808.
[24] C. Xiao, S. Li, x. Zhang, D. MacFarlane, MnO_2/$MnCo_2O_4$/Ni heterostructure with quadruple hierarchy: a bifunctional electrode architecture for overall urea oxidation, J. Mater. Chem. A 5 (2017) 7825–7832.
[25] B.K. Boggs, R.L. King, G.G. Botte, Urea electrolysis: direct hydrogen production from urine, Chem. Commun. 0 (2009) 4859–4861.
[26] N.S. Nguyen, G. Das, H.H. Yoon, Nickel/cobalt oxide-decorated 3D graphene nanocomposite electrode for enhanced electrochemical detection of urea, Biosens. Bioelectron. 77 (2016) 372–377.
[27] T. Fujimori, A. Morelos-Gómez, Z. Zhu, H. Muramatsu, R. Futamura, K. Urita,